

ADVANCED MODELING OF MICROMIRROR DEVICES

7/11/4

M. Adrian Michalicek, Darren E. Sene, and Victor M. Bright

Department of Electrical and Computer Engineering
Air Force Institute of Technology
Wright-Patterson AFB, Ohio 45433-7765

ABSTRACT

The Flexure-Beam Micromirror Device (FBMD) is a phase-only piston style spatial light modulator demonstrating properties which can be used for phase adaptive-corrective optics. This paper presents a complete study of a square FBMD, from advanced model development through final device testing and model verification. The model relates the electrical and mechanical properties of the device by equating the electrostatic force of a parallel-plate capacitor with the counteracting spring force of the device's support flexures. The capacitor solution is derived via the Schwartz-Christoffel transformation such that the final solution accounts for non-ideal electric fields. This complete model describes the behavior of any piston-style device, given its design geometry and material properties. It includes operational parameters such as drive frequency and temperature, as well as fringing effects, mirror surface deformations, and cross-talk from neighboring devices. The steps taken to develop this model can be applied to other micromirrors, such as the Cantilever and Torsion-Beam designs, to produce an advanced model for any given device.

The micromirror devices studied in this paper were commercially fabricated in a surface micromachining process. A microscope-based laser interferometer is used to test the device in which a beam reflected from the device modulates a fixed reference beam. The mirror displacement is determined from the relative phase which generates a continuous set of data for each selected position on the mirror surface. Plots of this data describe the localized deflection as a function of drive voltage.

INTRODUCTION

A growing trend in optical processing and related fields is the implementation of micromirror-based spatial light modulators (SLMs) for various optical applications [1]. The Flexure-Beam Micromirror Device (FBMD) is a phase-only piston style SLM demonstrating properties which can be used for phase adaptive optics. High optical efficiency and individual micromirror addressability make large arrays of devices well suited to phase-front modulation applications [2,3]. For example, Fig. 1 shows an array of devices used to discretely lengthen or shorten the optical path of incoming light to correct for phase-front aberrations. Other designs of micromirrors, such as the Cantilever or Torsion-Beam devices, have become increasingly favorable for applications in which a redirection of incoming light is desired.

The micromirrors studied in this paper were commercially fabricated using a standard polysilicon micromachining process. In this paper, ideal models are developed for all three designs. Additionally, an advanced model is developed for the FBMD which accounts for surface deformations, fringing losses, and cross-talk from neighboring devices as well as operating conditions such as temperature and drive frequency. The steps taken in this

process can be applied to other designs of micromirrors in order to create advanced models for any given device. The model is verified with a microscope-based laser interferometer used to study the behavior of the micromirror devices.

The FBMD, shown in Fig. 2(a), is a $60 \times 60 \mu\text{m}$ square mirror with flexures attached at the corners spanning two sides of the mirror. The actuation of the device is electrostatic such that a voltage is applied to an address electrode beneath the mirror creating a potential difference between this electrode and the mirror which is grounded. This creates a downward electrostatic force on the mirror which is counteracted by an upward spring force of the flexures. Figure 2(b) represents the actuation and characteristic behavior of the device illustrating these forces.

COORDINATE SYSTEM AND VARIABLES

A convenient characteristic of most micromirror devices is the symmetry designed about the center of the device. Most micromirror devices are designed in the shape of squares or other polygons that share similar symmetric traits. Therefore, a simple Cartesian coordinate system can be assigned to analyze the behavior of micromirror devices which makes use of this symmetry. As shown in Fig. 3(a), the x and y axes lie in the plane of the top of the address electrode and intersect at the center of the device. The z axis defines the vertical dimension within the device. The mirror widths along the x and y axes, w_x and w_y respectively, are shown such that the coordinates used to describe a position along the mirror surface range from negative to positive values of half the width. This coordinate system will help simplify the solutions of symmetric physical properties such as the electric field intensity which is uniform only at the center of the device.

In order to describe the mechanical behavior of micromirror devices, a set of variables must be defined that fully accounts for the physical geometry and motion of the mirrors and flexures. These variables are graphically defined using a simple micromirror device consisting of two flexures supporting the device at opposite ends of the mirror. The flexures and support posts are shown separated from the mirror for the purpose of clarification between the resting and actuated positions of the device.

The flexure variables shown in Fig. 3(b) are comprised of the initial deflection due to gravity, d_g , the actuated deflection at the end of the flexures, d_f , the resting separation distance between the mirror and address electrode, z_o , the actuated separation distance at the end of the flexures, z_f , and the spacer thickness, t_s , used in the fabrication of the device. The mirror variables shown in Fig. 3(a) are a function of position along the surface of the mirror and include the vertical separation distance between the mirror and address electrode, $z_m(x,y)$, and the surface distribution of mirror position relative to the ideal uniform deflection, $\Delta z(x,y)$. This includes mirror surface deformations and tilting of the mirror due to cross-talk or variances in the spring constants of each flexure.

The initial deflection due to gravity can be found using the combined mass of the mirror, M , and the characteristic spring constant of the device, k , such that

$$d_g = \frac{Mg}{k} \quad (1)$$

where g is the acceleration constant due to gravity. If the spring constants of each flexure are known to be unequal, this deflection can be found for each flexure using its portion of the total weight of the mirror. For the purpose of simplicity, however, it is assumed that each flexure of a given device is identical.

As shown in Fig. 3(b), the resting position of the device at the end of the flexures, z_o , is given by:

$$z_o = t_s - d_g = d_f + z_f \quad (2)$$

which describes the vertical separation distance between the address electrode and the mirror at the end of the flexures when no address potential is applied. Likewise, as shown in Fig. 3(a), the separation of the mirror and address electrode is given as

$$\begin{aligned} z_m(x, y) &= z_o - d_f - \Delta z(x, y) \\ &= z_f - \Delta z(x, y) \end{aligned} \quad (3)$$

The most important relationship defines the relative deflection as a function of position along the mirror surface, $d(x, y)$, such that

$$d(x, y) = d_f + \Delta z(x, y) \quad (4)$$

which describes the deflection observed for a given voltage at any point (x, y) along the surface of the mirror. Ultimately, this is the independent variable used to characterize a micromirror device such that this deflection is plotted against the address voltage.

ELECTROSTATIC ACTUATION

In order to compute the electrostatic force on the mirror, it must first be determined by which means this force will be calculated. More specifically, it must be decided whether the charge distribution, which is not uniform over the mirror surface, will be considered. The charge distribution will change with the position of the mirror surface and will also be altered by any mirror surface deformations or discontinuities such as etch holes. This leads to a complicated solution when integrating across the mirror. As an alternative, since both the charge distribution of the mirror and the applied electrode voltage are related to the electric field within the device, it is possible to express the potential energy, ξ , of the electric charge distribution solely in terms of this field such that

$$\xi = \frac{1}{2} \int_A \sigma V dA = \frac{1}{2} \int_v \epsilon_0 E^2 dv \quad (5)$$

where σ is the surface charge distribution on the mirror, V is the voltage between the mirror and electrode, A is the area of the mirror, ϵ_0 is the free space dielectric constant and E is the electric field intensity at any point in the volume v within the device [4]. By assigning a relative electric energy density of $\frac{1}{2}\epsilon_0 E^2$ to each point in space within the device, the physical effect of the charge distribution on the mirror surface is preserved. From this approach it is easy to see that the non-uniform charge distribution on the mirror surface and the fringing effects of electric fields around the edges of the mirror are complementary descriptions of the same electrical phenomenon.

With the ability to express the energy of the device in terms of the electric field, the electrostatic force on the mirror surface is

determined by a method known as virtual work [4]. This theory states that the change in the electrical energy of a capacitor is equal to the sum of the mechanical work done by displacing the plates and the change in the electrical energy of the source. The total electrostatic force of an ideal capacitor was determined to be

$$F = \frac{\epsilon_0 E^2}{2} A \quad (6)$$

which represents the total force on the surface of the mirror as a function of electric field. It also demonstrates that the force per unit area on the mirror surface is equal to the electrical energy density per unit volume within the micromirror device [4].

This relationship holds for non-uniform electric fields as well. The fringing electric field around the perimeter of the device alters the force per area on the mirror as a function of position on the mirror surface. The total electrostatic force acting on the mirror is

$$F = \iint f(x, y) dx dy = \frac{\epsilon_0}{2} \iint E^2(x, y) dx dy \quad (7)$$

The fringing electric field will diminish the force per unit area around the edges of the mirror and will produce a total electrostatic force that is slightly less than the ideal force calculated by neglecting fringing effects.

IDEAL FLEXURE-BEAM MODEL

Since the electric field is symmetric about the center of the device and the mirror and electrode are assumed to be rigid, the electric field lines along the outer edges of the cell shall be assumed uniform as well. Therefore, the induced electric field is initially assumed to be uniform and orthogonal to both the mirror and electrode at all points along both surfaces. This neglects deformations of the mirror surface during operation as well as fringing effects of the electric field around the edges of the device. The total electrostatic force of the Flexure-Beam device, F_{FB} , is found by the method of virtual work and reduces to:

$$F_{FB} = \frac{\epsilon_0}{2} E_{FB}^2 A \quad (8)$$

where E_{FB} is the ideal electric field, ϵ_0 is the free space dielectric constant, and A is the surface area of the mirror. The uniform separation distance between the address electrode and mirror, z_m , is given in Eq. (3) in which $\Delta z(x, y) = 0$ such that:

$$z_m = z_o - d_f \quad (9)$$

where z_o is the resting separation when no electrode voltage is applied and d_f is the vertical displacement of the mirror at any point along the surface.

The total force is found by substituting Eq. (9) into the expression for the ideal electric field, E_{FB} , in Eq. (8) which yields the magnitude of the downward force applied on the mirror:

$$F_{FB} = \frac{\epsilon_0}{2} \left(\frac{V}{z_o - d_f} \right)^2 A \quad (10)$$

The restoring force produced by a spring displaced a distance, d_f , from its equilibrium position is given by Hooke's Law:

$$F_s = kd_f \quad (11)$$

where k is the characteristic spring constant distinct to a particular spring system. This constant is distinct to each spring and can be

measured experimentally or determined using mechanical analysis. It is obvious that the linear response of the restoring force is valid only for a limited range of displacement distances. Forces greater than some critical force applied to the mirror must be avoided to ensure that the flexures do not deform and that the restoring force exhibits a linear response.

It is expected that the flexures will deform linearly. Therefore, balancing the upward restoring force of the micromirror flexures against the downward force of the parallel plate capacitor:

$$F_{FB} = F_s, \quad \frac{\epsilon_0}{2} \left(\frac{V}{z_0 - d_f} \right)^2 A = k d_f \quad (12)$$

produces an equality that can be solved to determine the necessary voltage, V , to vertically displace the mirror a desired distance, d_f from the resting position:

$$V = (z_0 - d_f) \sqrt{\frac{2 k d_f}{\epsilon_0 A}} \quad (13)$$

In this ideal model, the deflection along the mirror surface is assumed to be uniform. In a more realistic model, surface deformations invalidate this assumption and other non-ideal effects of geometry and device operation must be included as well.

As described above, the characteristic spring constant, k , can be experimentally determined for a specific micromirror device. However, mechanical analysis of the geometry and material properties comprising the flexures can approximate this value. As a result, the behavior of a Flexure-Beam Micromirror Device can be obtained without the need for experimental observations.

IDEAL CANTILEVER MODEL

The Cantilever micromirror device can be modeled using the same ideal conditions assumed for the Flexure-Beam micromirror device. Unlike the FBMD, however, the deflection is not uniform along the surface of the mirror, but a function of position along one dimension since the device tilts away from the support post. Assuming no surface deformations, the deflection becomes a linear function of position. Figure 4(a) illustrates the motion of the device and defines the dimension variables. It is known that the flexures will deflect according to Hooke's Law given in Eq. (11), but another aspect of the Cantilever device is the additional bending of the flexure which determines the angle of deflection, θ , at which the mirror is tilted.

As the mirror deflects downward, the force distribution along the surface of the mirror is no longer uniform since the end of the mirror is closer to the address electrode than elsewhere along the mirror. As a result, the total electrostatic force applied to the device will change according to the vertical deflection of the flexure, d_f and the angle of deflection, θ . To account for this behavior, two spring constants are introduced such that

$$F_s = k_1 d_f, \quad \theta = k_2 d_f \quad (14)$$

where k_1 describes the vertical deflection at the end of the flexure and k_2 describes the angle of mirror deflection. Both constants are directly related to the amount of electrostatic force acting on the device since they determine the position of the mirror.

The electrostatic force acting on the mirror is found by integrating the linear force distribution across the surface of the mirror. Since this force distribution is uniform in the y dimension, the force is only dependent on the integral over the x domain. Likewise, the separation distance between the mirror and address

electrode, z_m , and the vertical deflection distance of the mirror, d , are functions of x and are defined as

$$z_m(x) = z_0 - d_f - x \sin(\theta) \quad (15)$$

$$d(x) = d_f + x \sin(\theta) \quad (16)$$

The total electrostatic force for a Cantilever micromirror device, F_C , is found to be [5]

$$F_C = \frac{\epsilon_0}{2} w_y V^2 \int_0^{w_z} \frac{dx}{z_m^2(x)} = \frac{\epsilon_0 A V^2}{2 z_f z_t} \quad (17)$$

where the vertical separation distances at the flexure end of the mirror and tip of the device, z_f and z_t respectively, are shown in Fig. 4(a) and are defined as

$$z_f = z_0 - d_f, \quad z_t = z_f - w_x \sin(\theta) \quad (18)$$

Using the deflection relationships of Eqs. (14) and (16), the angle of deflection, θ , becomes

$$\theta = k_2 d_f = k_2 [d - x \sin(\theta)] \quad (19)$$

Since the length of the micromirror device is significantly larger than the separation distance between the mirror and address electrode, the angle produced by the actuation of the device is sufficiently small to allow for an approximation such that

$$\theta \approx \sin(\theta) = \frac{k_2 d}{(k_2 x + 1)} \quad (20)$$

Equating the electrostatic force in Eq. (17) with the restoring spring force of Eq. (14) yields the ideal characteristic model of the Cantilever micromirror device:

$$V = \sqrt{\frac{2 k_1 [d - x \sin(\theta)] z_f z_t}{\epsilon_0 A}} \quad (21)$$

where the address potential, V , is required to deflect a device some distance, d , at some position, x , along the surface of the mirror. Similar to the FBMD model, the spring constants of the Cantilever device can be found from mechanical analysis of the deflection and bending properties of the material comprising the flexure.

IDEAL TORSION-BEAM MODEL

The Torsion-Beam model is similar to the Cantilever model with the exception that only the rotational constant need be considered. The operation of the device is shown in Fig. 4(b) which illustrates that the ideal motion of the mirror does not include a deflection at the flexures. Therefore, the torque produced by an electrode on one side of the device, τ , is directly related to the angle of rotation of the mirror surface, θ , such that:

$$\tau = k \theta = F \bar{x} \quad (22)$$

where F is the total electrostatic force produced by the electrode and \bar{x} is the centroid position at which it is located given by [5]

$$F_T = \int_{x_A}^{x_B} f(x) dx, \quad \bar{x} = \frac{1}{F_T} \int_{x_A}^{x_B} x f(x) dx \quad (23)$$

where x_A is the lateral position at which the edge of the address electrode is located and the ideal force distribution, $f(x)$, is given as:

$$f(x) = \frac{\epsilon_o W_y V^2}{2z_m^2(x)}, \quad z_m(x) = z_o - x \sin(\theta) \quad (24)$$

Using the following angle approximation for rotation

$$\theta \approx \sin(\theta) = \frac{d}{x} \quad (25)$$

where d is the desired deflection at some position x and solving for the address potential, V , in Eq. (24) yields the ideal model:

$$V = \sqrt{\frac{2kd^3/\epsilon_o W_y x^3}{\ln\left(\frac{z_o - \frac{dW_x}{2x}}{z_o - \frac{dx_A}{x}}\right) + \left(\frac{z_o}{z_o - \frac{dW_x}{2x}}\right) - \left(\frac{z_o}{z_o - \frac{dx_A}{x}}\right)}} \quad (26)$$

which produces singularities at the center of the mirror, $x = 0$, since ideally no deflection can occur at that position [5]. Likewise, a limiting factor must be used so that the model does not predict a desired deflection past the point where the tip of the mirror would touch the substrate and prevent further rotation. The counterweight of the opposite side of the mirror is incorporated into the model by fitting the curve, via the spring constant, k , to the empirical data.

SPRING CONSTANTS

The flexures are modeled as simple springs in which the restoring force in the upward direction is linearly related to the vertical deflection of the mirror by a spring constant that can be determined from the geometry and material properties of the flexures. Furthermore, the mirror and flexures of the device comprise an undamped harmonic oscillator when the device is actuated with a periodic voltage at low frequencies. As a result, the restoring force of the flexures is not only a function of geometry and material properties, but also of temperature and driving frequency. At higher frequencies, however, squeeze film damping may become increasingly significant as the mirror must force air out of the volume of the device during operation.

To analyze the behavior of the flexures, another beam is rigidly supported on one end and free-floating on the other. A force, F , acts in the downward direction at the end of the beam where the maximum deflection, d , from the horizontal is known. The relation between force and deflection produces the cross sectional spring constant, k_{cs} , such that

$$d = \frac{FL^3}{3EI}, \quad I = \frac{1}{3}wt^3, \quad k_{cs} = \frac{Ewt^3}{L^3} \quad (27)$$

where L , w , t , and E are the length, width, thickness, and modulus of elasticity for the beam, respectively [6].

In addition to standard beam theory, the spring constant of the flexures must account for their layout such that a corner will produce a flexure that is more resistant to deflection than one of the same length that is straight. Therefore, a torsional spring constant must be added. As shown in Fig. 2(a), the square FBMD has flexures which span half the perimeter of the device and have several turns in their layout. The torsional spring constant must be evaluated for each corner of the flexure where L_1 and L_2 are the lengths of the primary and secondary portions of the flexure under

consideration respectively. The torsional angle through which the primary flexure is rotated by the secondary flexure, ϕ , is given as:

$$\phi = \frac{F_2 L_1 L_2 \sin(\theta)}{KG} = \frac{L_1}{(L_1 + L_2)} \frac{d_2}{L_2}, \quad G = \frac{E}{2(1+\nu)} \quad (28)$$

where

$$K = wt^3 \left[\frac{1}{3} - \left(\frac{0.21t}{w} \right) \left(1 - \frac{t^4}{12w^4} \right) \right] \quad (29)$$

and F_2 is the force observed at the end of the secondary portion of the flexure, d_2 is the deflection at the same position, θ is the planar angle between the two portions, and G is the shear modulus of the flexure material. The approximation of ϕ is valid since the deflection observed by the primary portion of the flexure, d_1 , is much smaller than the lengths of both portions of the flexures [7]. Solving for the relationship between force and deflection yields the torsional spring constant for a given portion of the flexure:

$$k_t = \frac{KE}{2(L_1 + L_2)L_2^2(1+\nu)\sin(\theta)} \quad (30)$$

There is also a stress term that can be added, k_s , given as:

$$k_s = \frac{\sigma(1-\nu)wt}{2L} \quad (31)$$

where σ and ν are the stress and Poisson ratio of the flexure material, respectively [8]. The system spring constant, k , is found by summing these constants per flexure, k_f , and multiplying by N , the number of flexures for a given device:

$$k = N(k_f) = 4[k_{cs} + k_t + k_s] \quad (32)$$

This constant is a function of temperature since the elastic modulus decreases as temperature increases and the thermal expansion of the flexures will slightly alter their geometry. This constant will be used to extract the elastic modulus as a function of temperature.

SCHWARTZ-CHRISTOFFEL TRANSFORMATION

The electrostatic force of the device is developed using a conformal mapping technique known as the Schwartz-Christoffel transformation. In any map of an electric field, the electric flux and equipotential lines are orthogonal to each other and form curvilinear squares between points of intersection. The sides of these squares will be perfectly linear for uniform electric fields and curved for any non-uniform field. As shown in Fig. 5, the electric field is taken from an original complex plane $\gamma = x + iz$ which describes some polygon and transformed to a complex plane W , where W is an analytic function of γ . This transformation preserves the orthogonal nature of the flux and equipotential lines and alters the sides of the curvilinear squares thus mapping the electric field to the W plane. It provides the means to determine the functional relationship between the two planes such that any electric field can be mapped about any geometry given the initial polygon [9].

The fringing electric field is analyzed using a parallel plate capacitor whose plates extend to infinity along the y axis and for negative x values. This symmetry approach is valid since the fringing effects of the device are localized at the outer edges of the mirror. Transforming a finite plate capacitor results in a solution with several elliptic integrals which is virtually unusable for further calculations [9]. The Schwartz-Christoffel transformation is a widely-accepted tool for such analysis which describes the initial polygon in terms of the exterior angles about which its perimeter

traverses and the points at which the angle is located. The conformal mapping equation is given as:

$$\gamma = \gamma_o + A \int (w - b_o)^{\alpha_0} (w - b_1)^{\alpha_1} \dots (w - b_n)^{\alpha_n} dw \quad (33)$$

where γ_o and A are constants determined by boundary conditions, b is the value of each point mapped into the W plane, and n is the number of points mapped into finite values. The quantity exponents, $\alpha = \theta/\pi - 1$, are functions of the external angle, θ , of the transformed polygon at each mapped point in the γ plane [9,10].

The electric field of a parallel plate capacitor originally drawn in the γ plane is shown in Fig. 5(a) where the points being mapped into the W plane are labeled A through D and are enclosed by the polygon drawn around the upper and lower plates of the capacitor. Figure 5(b) represents the mapping of these points in the W plane showing the finite values of points B , C , and D . The constant electric flux lines are mapped into W circularly about point C which produces the relationship:

$$W = \Psi + i\Phi = \left(\frac{V}{i\pi} \right) \ln(w), \quad w = \exp\left(\frac{i\pi W}{V} \right) \quad (34)$$

where Ψ and Φ represent electric flux and potential respectively, V is the potential applied to the capacitor and w represents the W plane in polar form. Evaluating the exponents at each mapped point, $\alpha_B = \alpha_D = 1$ and $\alpha_C = -1$, the transformation becomes:

$$\gamma = \gamma_o + A \int \frac{w^2 - 1}{w} dw = \gamma_o + A \left[\frac{1}{2} w^2 - \ln(w) \right] \quad (35)$$

Applying the boundary conditions at points B and D in both planes, the constants of the transformation are $\gamma_o = -\frac{1}{2}A$ and $A = -(z_m/\pi)$ which produces the final relationship:

$$\gamma = x + iz = \frac{z_m}{\pi} \left[\frac{i\pi}{V} W + \frac{1}{2} \left(1 - \exp\left(\frac{2\pi i W}{V_o} \right) \right) \right] \quad (36)$$

This can be solved for the real and imaginary parts to produce the parameterized solution in two dimensions for the edge of a parallel plate capacitor. Doing so yields

$$x = \frac{z_m}{2\pi} \left[\psi + 1 - e^\psi \cos(\varphi) \right] \quad (37)$$

$$z = \frac{z_m}{2\pi} \left[\varphi - e^\psi \sin(\varphi) \right] \quad (38)$$

where z_m is the vertical position of the mirror above the address electrode. The index parameters ψ and φ are normalized functions of flux and potential respectively, such that

$$\psi = -\frac{2\pi\Psi}{V}, \quad -\infty \leq \psi \leq \infty \quad (39)$$

and

$$\varphi = \frac{2\pi\Phi}{V}, \quad 0 \leq \varphi \leq 2\pi \quad (40)$$

where Φ is the potential variable, Ψ is the electric flux variable, and V is the potential applied between the mirror and electrode. The result of Eqs. (37) and (38) is plotted in Fig. 6(a) which demonstrates that the fringing effects are only present at the edges of the mirror. Moving toward the center of the device, away from the edges of the mirror, the electric field and equipotential lines approach ideal uniformity. The fringing effects are only considered for field lines on the underside of the mirror ($\psi \leq 0$) since

neighboring micromirror devices prevent the extended fringing that would produce field lines emanating from the top of the mirror and underneath the electrode. Micromirror devices standing alone may experience a larger fringing loss than devices positioned within an array due to the existence of these extending electric field lines.

For devices standing alone, the electrostatic force along the electric field lines outside the device acts in the opposite direction as those within the device. Although the arc lengths of these lines are much larger and thus the electric intensity much weaker, the net electrostatic force of these lines should not be neglected. Integrating this solution along the top of the mirror produces some non-zero force in the upward direction that counters the actuation of the device. The net electrostatic force acting on devices standing alone is somewhat less than that on devices within an array.

ELECTRIC FIELD INTENSITY

To find the electric field intensity as a function of position along the mirror surface, the length of the arc traced along a constant electric flux value must be determined. Recognizing that differential change in the potential function, $d\varphi$, will result in differential change in position, dx and dz , the relation is found to be

$$dl = \sqrt{dx^2 + dz^2} = \sqrt{\left(\frac{dx}{d\varphi} \right)^2 + \left(\frac{dz}{d\varphi} \right)^2} d\varphi \quad (41)$$

where dl is the differential change in the arc length. Using the parameterized solution of x and z to find the derivatives with respect to the potential function, φ , and integrating yields

$$l = \frac{2z_m}{\pi} (1 + e^\psi) \int_0^{\frac{\pi}{2}} \left[1 - m \sin^2 \theta \right]^{\frac{1}{2}} d\theta, \quad m = \frac{4e^\psi}{(1 + e^\psi)^2} \quad (42)$$

which is simply an elliptic integral of the second kind where the need for $m \leq 1$ is valid for all values of ψ . Therefore, the elliptic integral series solution is

$$l = z_m (1 + e^\psi) \left[1 - \sum_{n=1}^{\infty} \left[\left(\prod_{k=1}^n \frac{2k-1}{2k} \right)^2 \frac{m^n}{2n-1} \right] \right] \quad (43)$$

which is somewhat difficult to use for real-time modeling due to the recursive multiplication and the need for a large number of terms to converge to a solution [5,11].

As an alternative to the elliptic integral series solution, two approximations were developed that are far more efficient and simpler to employ. First, the numerical integration of Eq. (43) produces a series solution that converges much more quickly and requires significantly fewer terms to maintain a certain degree of accuracy. Another approximation is a curve-fitting approach which produces a closed-form solution in the form of an exponentially increasing function. For all calculations, however, the arc lengths were evaluated by finding the converging limit of Eq. (43) with at least $N = 500$ terms in order to minimize error propagation.

With the address electrode at some potential, V , and the mirror grounded, the field intensity at a position, x , along the mirror is

$$E = \frac{V}{l}, \quad x = \frac{z_m}{2\pi} [\psi + 1 - e^\psi] + \frac{w_x}{2} \quad (44)$$

which parametrically represents the electric field intensity as a function of position over half the mirror ($0 \leq x \leq \frac{1}{2}w_x$) where w_x is the width of the mirror in the x direction.

To project this solution into the y domain as well, algebraic averaging was used such that the net electric field intensity at some position along the surface of the mirror is the average of that given by the x and y coordinates.

$$E_{xy} = \frac{1}{2}[E_x + E_y] \quad (45)$$

where the x and y coordinates are evaluated as:

$$x = \frac{z_m}{2\pi}[\psi_x + 1 - e^{\psi_x}] + \frac{w_x}{2} \quad (46)$$

$$y = \frac{z_m}{2\pi}[\psi_y + 1 - e^{\psi_y}] + \frac{w_y}{2} \quad (47)$$

The normalized magnitude of the electric field along the surface of the mirror is shown in Fig. 6(b) as a function of x and y over one quarter of the mirror surface. At the center of the mirror, no fringing effects exist and the ideal uniform electric field is shown. At the edges, however, the fringing effects are quite significant. At the corners of the mirror and address electrode, the electric field intensity is reduced to 78.7% of the ideal magnitude. The solution in one dimension, given in Eq. (44), is the cross section along the diagonal of the solution in two dimensions.

To determine the total electrostatic force acting on the mirror in the downward direction, as given in Eq. (7), the square of the electric field intensity in Eq. (45) must be numerically integrated across the mirror surface using the flux parameter, ψ . It is obvious that the total force will be less than the ideal force calculated using an ideal uniform electric field. The total force becomes

$$\begin{aligned} F_{FB} &= \frac{\epsilon_0}{2} \int_{-\frac{w_x}{2}}^{\frac{w_x}{2}} \int_{-\frac{w_y}{2}}^{\frac{w_y}{2}} [E_{xy}]^2 dy dx \\ &= \frac{\epsilon_0 w_y}{4} \int_0^{\frac{w_x}{2}} E_x^2 dx + \epsilon_0 \int_0^{\frac{w_x}{2}} \int_0^{\frac{w_y}{2}} E_x E_y dy dx \\ &\quad + \frac{\epsilon_0 w_x}{4} \int_0^{\frac{w_y}{2}} E_y^2 dy \end{aligned} \quad (48)$$

Each of these integrals must be numerically integrated individually due to their distinct integrands. In order to do so, the corresponding parameter, ψ , is divided into N segments which are used to evaluate discrete samples of the electric field intensity and position. The definite integral is evaluated as the sum of the area of rectangles formed in this process. For example, the following integral is numerically integrated such that

$$\int_0^{\frac{w_x}{2}} E_x dx = \frac{1}{2} \sum_{i=1}^N [(x_i - x_{i-1})(E_i + E_{i-1})] \quad (49)$$

where the height of the rectangle is defined as the average of the values of the electric field intensity at each side of the rectangle. The remaining integrals are evaluated using the converging limit of the series solution generated by this technique.

The range of parameter values must be chosen to correspond to the range of integration over position. In order to do so, a relationship must be developed between the index parameter, ψ , and the center of the mirror, $x = 0$. Moving away from the edges of the device, the index parameter becomes increasingly negative.

Therefore, Eq. (37) can be reduced and solved for the index parameter at the center of the device, ψ_o , such that

$$x = 0 = \frac{z_m}{2\pi}[\psi_o + 1] + \frac{w_x}{2}, \quad \psi_o = -\left[\frac{w_x \pi}{z_m} + 1\right] \quad (50)$$

The index parameter at $y = 0$ is determined using the same technique. Since it is known that the value of the index parameter at the edge of the device is zero, the resulting range in the index parameter can be used to describe the desired range of integration with respect to position over the surface of the mirror.

ELECTRIC FIELD FRINGING LOSSES

The parametric numerical integration was performed for numerous values of device dimensions, w_x and w_y , and mirror separation distance, z_m , such that an analytic equivalent of this approach could be determined. It was found that the fringing losses are best described as a fractional loss in the ideal force:

$$\Delta f_{FL} \approx \frac{z_m}{165.4} \left[\frac{2(w_x + w_y)}{w_x w_y} \right], \quad 0 < \Delta f_{FL} < 1 \quad (51)$$

This approximation function is shown in Fig. 7 along with the results of numerical integration. It is obvious that as the mirror area increases, the effects of fringing decrease, thus smaller devices are more affected by such losses to the extent that the ideal solution can not be used. It should be noted that Eq. (51) is valid for other device geometries such that the quantity in brackets is the ratio of the length of the perimeter to the area of the mirror.

Another reduction in the magnitude of the ideal force of a capacitor is the unused area in the surface of the mirror devoted to etch holes. The fractional loss is simply a ratio of the total etch hole area to the ideal area of the device. When this is added to the fringing loss, Δf_{FL} , the total loss, Δf , describes the reduction of the ideal electrostatic force of the device due to such non-ideal characteristics. The net electrostatic force acting on the surface of the mirror in the downward direction becomes

$$F = \frac{\epsilon_0}{2} [1 - \Delta f] \iint \left(\frac{V}{z_m(x,y)} \right)^2 dxdy \quad (52)$$

where $z_m(x,y)$ represents the vertical separation distance between the electrode and mirror at any given position within the device and will not be uniform due to mirror surface deformations.

CROSS-TALK INTERFERENCE

Another characteristic of the electric field within a device is the interference produced by the electric field lines of neighboring devices. This could alter the electrostatic force on the mirror in two ways. First, the fringing field lines of one device can be distorted by partially conforming to those of another which would change the amount of fringing losses as calculated above. However, since the flexures and support posts between each device are grounded with the mirrors and a gap exists between these geometric features, the electric field fringing loss at the edge of an individual mirror is still dominated by the fringing effects within the device itself.

The second cross-talk effect would be the added force on the mirror supplied along additional field lines emanating from the electrode of a neighboring device. This interference is only present when the primary device is not actuated since the creation of a much stronger electric field within the primary device would

prevent the interference field. As shown in Fig. 8, the mirror of a primary device experiences a small force along the electric field lines from the first of four neighboring device that are actuated. If the address potential of the primary device, V_p , is approximately zero, the net cross-talk force supplied along the electric field lines is simply the integral of the linear force distribution along the surface of the mirror. This distribution is determined by the address potential of the neighboring device, V_1 , the length of each electric field line, L , and the angle of the force vector, θ . The length of the electric field lines is given by

$$L(x) = \sqrt{(\Delta x^2 + z_o^2)} = \sqrt{\left(x + x_s + \frac{w_x}{2} \right)^2 + z_o^2} \quad (53)$$

where x_s is the separation distance between each device as shown in Fig. 8 which also shows Δx as the horizontal distance between the neighboring address electrode and any point along the surface of the primary mirror. The linear force distribution is found to be

$$f_1(x) = \frac{\epsilon_o}{2} w_y \left(\frac{V_1}{L(x)} \right)^2 \cos(\theta) = \frac{\epsilon_o}{2} \frac{w_y V_1^2 z_o}{[L(x)]^3} \quad (54)$$

which is not a function of position in the y direction. Since this distribution is not symmetric about the center of the device, the side of the mirror nearest the neighboring device will experience a greater force than the opposite side of the mirror. In order to determine the amount of force at both ends of the device, the centroid position, \bar{x}_1 , and the total force due to cross-talk, F_1 , must be found and are defined as [5]

$$F_1 = \int_{-w_x/2}^{w_x/2} f_1(x) dx, \quad \bar{x}_1 = \frac{1}{F_1} \int_{-w_x/2}^{w_x/2} x f_1(x) dx \quad (55)$$

It is important to note that the centroid position, \bar{x}_1 , is not a function of address potential of the neighboring device, V_1 , due to the common symmetrical design of the devices within the array. Figure 9 illustrates the linear force distribution of the cross-talk interference for a single neighboring device and illustrates the total force at the centroid position. In one dimension, shown in Fig. 9, the resulting force observed by the flexures supporting each end of the device, F_a and F_b , determines the deflection at each end which will not be equal. The end of the device nearest the actuated neighbor will deflect more than the other. The force at each flexure is proportional to F_1 such that

$$F_a = F_1 \left(\frac{a_x}{w_x} \right), \quad F_b = F_1 \left(\frac{b_x}{w_x} \right) \quad (56)$$

where

$$a_x = \frac{w_x}{2} + \bar{x}_1, \quad b_x = \frac{w_x}{2} - \bar{x}_1 \quad (57)$$

These forces are directly related to the deflection at each end by the spring constant of the flexure.

Expanding this analysis into two dimensions, it is known that the y centroid falls on the x axis due to the device symmetry. The total force due to cross talk from the first device, F_1 , is localized at $(x, y) = (\bar{x}_1, 0)$ and produces a net downward force at each of the four corners of the device. For a square device, the other three neighbors produce similar forces located at the same position, given in Eq. (55), relative to each mirror. The centroid positions of all four neighbors are shown in Fig. 10(a) as circles numbered

according to the corresponding device. The total force due to cross talk, F_{CT} , is centered at the final centroid position, $(\bar{x}_{CT}, \bar{y}_{CT})$, which is determined by the forces of the surrounding devices:

$$\bar{x}_{CT} = \frac{1}{F_{CT}} \sum_{n=1}^4 \bar{x}_n F_n, \quad \bar{y}_{CT} = \frac{1}{F_{CT}} \sum_{n=1}^4 \bar{y}_n F_n \quad (58)$$

where n is the index of the neighboring devices and F_{CT} is simply the sum of their forces. Similar to the analysis in one dimension, given in Eq. (56), the force observed at each corner of the device is proportional to the total force, F_{CT} , as a function of position relative to the centroid, $(\bar{x}_{CT}, \bar{y}_{CT})$. Figure 10(b) illustrates the final effect of cross-talk which shows the uneven tilting of the mirror in response to the location of the final centroid. In this example, the first and fourth devices are actuated more than the second and third devices which determines the position of the centroid and results in a tilting of the mirror.

The deflection of the mirror due to cross talk is a function of position across the mirror surface and can be obtained by developing an equation of the plane formed by joining the four corners. The function Δz_{CT} represents this deflection such that

$$\Delta z_{CT}(x, y) = \frac{D_{sum}}{4} + \frac{D_x}{2} \left(\frac{x}{w_x} \right) + \frac{D_y}{2} \left(\frac{y}{w_y} \right) + D_{xy} \left(\frac{xy}{w_x w_y} \right) \quad (59)$$

and the deflection coefficients are given as

$$\begin{aligned} D_{sum} &= d_A + d_B + d_C + d_D, \\ D_x &= d_B + d_C - d_A - d_D, \\ D_y &= d_A + d_B - d_C - d_D, \\ D_{xy} &= d_B + d_D - d_A - d_C \end{aligned} \quad (60)$$

where d_A , d_B , d_C , and d_D are the deflections at corners A , B , C , and D respectively. The amount of the cross-talk deflection, Δz_{CT} , increases as the distance between devices, x_s , decreases. Therefore, arrays containing micromirror devices in close proximity to each other may be significantly affected by neighboring devices.

To determine the effect of proximity, the maximum deflection of a primary device due to cross-talk, d_{max} , was found by fully actuating all neighboring devices. This analysis was completed for a variety of device separation distances, x_s , and primary mirror surface areas of a square mirror and was found to be:

$$d_{max} = \frac{4d_{2\pi}(z_o - d_{2\pi})^2}{z_o w} \left[\frac{(x_s + w)L_{min} - x_s L_{max}}{L_{min} L_{max}} \right] \quad (61)$$

where $d_{2\pi}$ is the 2π modulation deflection for any arbitrary wavelength, w is the width of the square mirror, and L_{min} and L_{max} are the minimum and maximum arc lengths between devices, respectively, shown in Fig. 8 and defined as:

$$L_{min} = \sqrt{x_s^2 + z_o^2} \quad (62)$$

$$L_{max} = \sqrt{(x_s + w)^2 + z_o^2} \quad (63)$$

This result is shown in Fig. 11 which illustrates that the effect of cross-talk is dramatically reduced as devices are placed further apart. However, devices in close proximity to each other were found to be susceptible to this interference. Since the actuation of the primary device dominates over the cross-talk interference from neighboring devices, the effects of cross-talk can be removed by setting a resting bias for the micromirrors so that their resting position is at some small deflection.

MIRROR SURFACE DEFORMATION

Another major factor in the behavior of the device is the deformation of the mirror surface during actuation. This behavior is compared to the deformation of a rigid beam supported on each end by ball supports such that the free-floating flexures allow the edges of the mirror to angle upwards as the center of the mirror deflects downward. The maximum deflection, δ , of the beam under a uniform force per unit length, q , is given by

$$\delta = \frac{5qL^4}{384EI}, \quad q = \frac{F}{L}, \quad I = \frac{1}{12}wt^3 \quad (64)$$

where L , w , t , and E are the length, width, thickness, and modulus of elasticity of the beam, respectively [6].

Although the edges of the beam are allowed to angle upward, the angles produced by very small deflections at the center of the beam compared to its length, $\delta \ll L$, are negligible. Therefore, the deformation is modeled as a beam rigidly supported at the ends and is represented as one period of a cosine wave having an amplitude equal to half the maximum deflection at the center of the beam, δ . Figure 12(a) represents this beam deflection. For a micromirror device of area A , the maximum surface deformation including an initial deformation due to gravity reduces to

$$\delta = \frac{FA}{(6.4)Et^3} = \left[\frac{\varepsilon_o}{2} \left(\frac{V}{z_m} \right)^2 A + Mg \right] \frac{A}{(6.4)Et^3} \quad (65)$$

where M is the combined mass of the mirror and g is the acceleration constant due to gravity. Using the above beam analysis, the deformation of the mirror surface becomes

$$z_m(x, y) = z_f - \delta \left[1 + \frac{1}{2} \left(\cos\left(\frac{2\pi x}{w_x}\right) + \cos\left(\frac{2\pi y}{w_y}\right) \right) \right] \quad (66)$$

where z_f is the vertical position of the flexures at the corners of the mirror. Figure 12(b) shows a surface plot of this function which depicts the maximum deflection along the surface ($z_f - 2\delta$) to be at the center of the mirror ($x = y = 0$). It should be noted that the elastic modulus for the mirror surface will be difficult to predict for devices with several layers of structural, adhesive, and reflective material. Likewise, the peak deflection coefficient, δ , does not include the effects of stress which can significantly alter the deformation behavior of larger devices.

For micromirror devices with the flexures attached at some point along the edge of the mirror, the solution in Eq. (66) is simply rotated and scaled down to fit within the dimensions of the mirror. The rotated coordinates of the solution are found to be

$$x' = s_x [x \cos(\theta_x) - y \sin(\theta_y)] \quad (67)$$

$$y' = s_y [x \sin(\theta_x) + y \cos(\theta_y)] \quad (68)$$

where the scale factors, s_x and s_y , and rotation angles, θ_x and θ_y , are determined by the geometry of the device and the position at which the flexures are attached. The scale factors must be included in order to generate a solution with areas of zero deformation at the flexures. If neglected, these areas would appear outside the geometry of the device and the model becomes discontinuous at the position of the flexures along the mirror.

The rotated coordinates given in Eqs. (67) and (68) are used in Eq. (66) to produce the contour plot shown in Fig. 13(b) in which

the original solution is shown within the dashed lines. The surface of the rectangular mirror where the flexures are attached has no deformation and is shown as white while deeper deformations are shown darker relative to their depth. This contour illustrates the effects of deformations at the corners of the mirror which are free to deform without rigid support by the flexures. In both solutions, the peak deformation is given as $z_f - 2\delta$ although the peak deformation of the rotated solution will be slightly less than the original solution shown in Fig. 13(a) since the center of the mirror is much closer to the flexures. Therefore, the deflection coefficient, δ , must be reduced. The surface deformation of any rectangular Flexure-Beam device can be represented with this solution.

FREQUENCY RESPONSE

Since the mirror is an oscillator, the spring constant directly determines the resonant frequency of the mirror given its mass. The time response of any harmonic oscillator can be found by solving a differential equation relating Newton's second law and Hooke's law to a sinusoidal driving force [12]. The solution is

$$z(t) = \frac{F_o \cos(\omega t)}{M \sqrt{(\omega_o^2 - \omega^2)^2 - 4\omega^2\beta^2}}, \quad \omega_o = \sqrt{\frac{k}{M}} \quad (69)$$

where $z(t)$ is the deflection of the oscillator in time, F_o and ω are the amplitude and frequency of the driving force, respectively, ω_o is the resonant frequency of the oscillator, k is the spring constant in Eq. (32), M is the combined mass of the mirror as determined from the densities and geometries of the materials comprising it, and β is the damping parameter of the device. The device experiences a squeeze-film damping effect by displacing the air within the device as it deflects. The peak deflection response of an oscillator is found by obtaining the maximum deflection of Eq. (69) as a function of frequency. The combined restoring force of the flexures simplifies to a frequency-dependent spring force given by

$$F_s = d_f \sqrt{[k - M(2\pi f)^2]^2 - 4M^2\beta^2(2\pi f)^2} \quad (70)$$

where d_f is the vertical deflection of the mirror at the flexures and f is the operating frequency of the device. For low operating frequencies, $(2\pi f \ll \omega_o)$, the force reduces to the static spring force of $F_s = k d_f$ given by Hooke's Law.

TEMPERATURE DEPENDENCE

The temperature effects are analyzed by considering the coefficients of thermal expansion for the materials comprising the flexures and mirrors. The length, width and thickness of the device components will increase with temperature which alters such factors as the spring constant of the flexures or the total electrostatic force on the mirror. Consider the length of the flexures as a function of temperature, T , in which

$$L = l_o [1 + \alpha(T - T_o)] \quad (71)$$

where l_o is any length at temperature T_o and α is the coefficient of thermal expansion for the flexure material [13]. The temperature dependence of the entire device can then be predicted by applying this analysis to all dimensions of length in the final model.

Additionally, the elastic modulus is a function of temperature where the device becomes more flexible as temperature rises. To find this relationship, the resonant frequency is obtained at various temperatures and Eqs. (32) and (69) are used to extract the spring constant and the elastic modulus as a function of temperature.

ADVANCED FLEXURE-BEAM MODEL

To develop the characteristic model for the device, the electrostatic force given in Eq. (52) is set equal to the spring force in Eq. (70) and solved for the address potential, V , such that

$$V = \sqrt{\left[\frac{2F_s}{\epsilon_o [1 - \Delta f]} \right] \left[\frac{1}{\iint z_m^{-2}(x, y) dx dy} \right]} \quad (72)$$

Recognizing that δ is a function of V as given in Eq. (62), this creates a circular reference when calculating the voltage required to deflect the device a desired distance. Therefore, the spring force is used to replace the electrostatic force given in this equation since these forces are ideally equal. The temperature and surface deformation effects then can be added such that:

$$V = \sqrt{\frac{2F_s}{\epsilon_o [1 - \Delta f]} \tan \left[\frac{(z_o - d - \Delta z(x, y) - \delta)^2}{w_x w_y [1 + \alpha_M (T - T_o)]^2} \right]} \quad (73)$$

where

$$F_s = (d - \Delta z(x, y)) \sqrt{[k_o - M(2\pi f)^2]^2 - 4M^2 \beta^2 (2\pi f)^2}, \quad (74)$$

$$k_o = \frac{k}{[1 + \alpha_F (T - T_o)]}, \quad (75)$$

$$\delta = \left[\frac{[k_o(d - \Delta z(x, y)) + Mg] w_x w_y}{(6.4) E t^3} \right] [1 + \alpha_M (T - T_o)] \quad (76)$$

and where α_F and α_M are the coefficients of linear expansion for the flexures and mirror respectively, d is the desired deflection distance at some location (x, y) on the mirror, and z_o is the resting height of the flexures. This height is related to the initial spacer thickness such that the initial deflection due to gravity is a result of the weight of the mirror related by the spring constant of the flexures. This model is valid as long as the desired mirror deflection is greater than the surface deformation at that point.

FABRICATION

The mirror arrays were commercially fabricated by the Microelectronics Corporation of North Carolina (MCNC) using the ARPA-sponsored Multi-User MEMS Process (MUMPS). This fabrication process has three structural layers of polysilicon and silicon dioxide as the sacrificial material. The first polysilicon layer, Poly-0, is non-releasable and is used for address electrodes and local wiring while the second and third layers, Poly-1 and Poly-2 respectively, can be released to form mechanical devices. The MUMPS process allows a layer of metal to be deposited only on the top of the Poly-2 layer. The metal is deposited as the last layer of the fabrication process since the metal is non-refractory and the polysilicon layers are annealed at 1100°C to reduce stress. These active layers are built up over a silicon nitride layer which insulates them from the conductive silicon substrate.

This process is illustrated using a simple device consisting of a metallized mirror, one flexure, and one support post. Note that this design does not use Poly-1. Figure 14(a) shows a cross-section of this design prior to metallization. After fabrication, the sacrificial layers must be etched away to release the mechanical layers.

Figure 14(b) shows the released structure after the metal has been deposited and the sacrificial material has been removed.

The unreleased die are delivered from MCNC in a protective photoresist which is stripped off in a three minute acetone bath. The die are then rinsed in deionized water for two minutes. The actual release etch is a two minute dip in concentrated (49%) hydrofluoric acid. The die are then rinsed for five minutes in gently stirred deionized water. After the rinse, they are soaked for five minutes in 2-propanol, then baked dry in a 150°F oven for five minutes. The propanol displaces the water, and when it evaporates its lower surface tension prevents the pull-down and destruction of the released polysilicon structures.

EXPERIMENTAL SETUP

The experimental setup is shown in Fig. 15 in which a microscope-based laser interferometer is used to modulate a fixed reference beam with the beam reflected from the device. An incident laser beam is split into a reference and object beam and each is allowed to travel some distance before they are joined together at an aperture to create an interference pattern. A photodetector placed behind this aperture produces a current which is linearly related to the intensity of the interference pattern. Along the path of the object beam, the path length increases by twice the vertical displacement of the device under test. Therefore, by using a periodic drive signal and knowing the exact wavelength of the incident laser beam, a continuous sample of the detector current yields an accurate measurement of the displacement of the micromirror surface. Comparing this displacement with the input signal yields the response characteristics of the device [14].

The microscope allows the object beam to be finely focused onto the surface of the mirror such that the spot size is approximately 4 μm in diameter. Since the translation stage supporting the device can be moved in increments of 0.1 μm, the displacement at any location on the mirror can be measured and compared to measurements taken elsewhere throughout the mirror surface. The result is a mapping of the surface deformations or tilting of the mirror as a function of applied potential. A system precision of 2 nm was measured using multiple characterization curves for a single location on one micromirror device.

An additional setup was used to measure the frequency response of the devices studied. A device under test is placed in a temperature-controlled evacuation chamber at 20 mTorr of pressure. A spectrum analyzer is used to measure the mechanical energy of the device using the principle of virtual work. A peak in the mechanical energy is observed at the resonant frequency of the device. The output, however, is relative only to the mechanical energy of the device and does not represent deflection. This procedure can produce accurate evaluations of the spring constant of a device given its resonant frequency and mirror mass.

PROCEDURES AND RESULTS

The ideal models were verified by characterizing the devices and fitting the curve to the data using the spring constant. Data was taken for the FBMD and the Cantilever devices, but not for the Torsion-Beam device because the model was developed after the test chip was sent to fabrication with no Torsion-Beam devices. The model and experimental data for the Cantilever device is shown in Fig. 16 and the Torsion-Beam model is shown in Fig. 17 which illustrates the behavior at several positions along the surface of the mirror. The slight error shown at the center of the Cantilever device in Fig. 16 can be partially attributed to the uncertainty in positioning the 4 μm laser spot. The ideal model of the FBMD is not shown. It was determined that a spring constant of 2.6 N/m accurately fit the curve to the experimental data.

The frequency response of the square FBMD was analyzed using a complex transfer function derived from the Fourier transform of Eq. (69) such that the phase response of the device is preserved. As shown in Fig. 18, which shows this theoretical behavior and mechanical data of the device in arbitrary units, there is a slight miscalculation of 40 Hz between the predicted and observed resonant frequency. This is due to the value used for the mass of the mirror in which the mass of the flexures was neglected.

Theoretically, the damping coefficient, β , can be found as a function of device area, A , mirror separation distance, z_m , and atmospheric pressure by finding the resonant frequency of several devices at various pressures. However, for this particular FBMD, the resonant frequency could not be achieved above 100 mTorr of pressure which indicates that the squeeze-film damping effects on Flexure-Beam devices is quite significant. Devices with lower resonant frequencies and other geometries may not be as affected.

The resonant frequency of the square FBMD was found at various temperatures at 20 mTorr of pressure. The resulting spring constant of each sample, from Eq. (69), was then used to extract the elastic modulus, from Eq. (32), as a function of temperature. This function is shown in Fig. 19 which demonstrates a linear behavior. This function for thin-film polysilicon was found to be

$$E = (-0.03225)T + (172.3931) \text{ GPa} \quad (77)$$

where T is the Kelvin temperature. The range of temperature could not be expanded due to the limits of the experimental setup. At colder temperatures, condensation from the humidity in the air prevented an accurate characterization of the device.

Tests were conducted to verify the cross-talk and mirror surface deformations. The cross-talk testing involved generating a behavior curve for a device at normal operation and then another curve while its surrounding devices were fully actuated. No significant changes in the behavior were observed which stands to verify the assumption that such cross-talk effects are negligible for this device due to the 18 μm separation distance within the array.

The peak surface deformation in the center of the device was predicted to be 5 nm and measured to be 7 nm. The predicted value is based on the modulus of elasticity for polysilicon extracted from other devices (168 GPa) and is also affected by the stress of the mirror which is comprised of three material layers. As a result, this exact value of deformation is somewhat difficult to predict.

In order to verify the advanced Flexure-Beam model, the square FBMD was driven by a 250 Hz signal ranging from zero to approximately 16 volts while the laser spot was positioned at the corner of the mirror. Comparing the input signal with the resulting phase curve, the device behavior is plotted in Fig. 20 which shows that the device created a 2π phase change in a $\lambda = 632.8 \text{ nm}$ HeNe laser, $d_f = 316.4 \text{ nm}$, with an address potential of 15.25 volts.

The theoretical behavior of the device, shown as a dashed line, is calculated using design dimensions and the modulus of elasticity, $E=168 \text{ GPa}$, determined from a separately fabricated device. The actual modulus of elasticity of a thin film material depends on the fabrication process, and the modulus can vary significantly. Unless the modulus is determined exactly for the device being modeled, the value for bulk silicon, or a value determined from another thin film polysilicon device, must be used as a starting point in the model. Given this uncertainty in the value of the modulus of elasticity, the model will produce a representative behavior for the device. However, by altering only the modulus of elasticity, the representative curve can be shifted to match the observed data.

CONCLUSION

As Fig. 20 illustrates, the characteristic model in Eq. (73) closely predicts the actual behavior of the device presented in this paper. It has also been found to model other devices of various geometries and materials with similar accuracy. The ideal models were found to closely describe the behavior of a large portion of the devices tested once the model was fit to the data by the spring constant. The material analysis performed in the advanced model seems to remove the need to empirically determine this constant.

Micromirror devices can be commercially fabricated in a variety of surface micromachining processes due to their simple, robust design. The ideal models presented in this paper can be used to describe the behavior of a large majority of devices based on their design and motion. For very large or very small devices, the advanced model may be required to characterize the device. These thresholds at which the advanced model should be used is defined by the size of the device and its fabrication process which incorporates other variables such as stress and thickness of various layers. An advanced model was developed for any rectangular piston-style Flexure-Beam Micromirror Device. An advanced model for other micromirror designs can be developed by following the same steps for a particular geometry and fabrication process.

REFERENCES

- [1] R. M. Boysel, J. M. Florence, and W. R. Wu, "Deformable mirror light modulators for image processing," in Proc. SPIE, vol. 1151, pp. 183-194, 1989.
- [2] R. H. Freeman and J. E. Pearson, "Deformable mirrors for all seasons and reasons," Applied Optics, vol. 21, pp. 580-588, Feb. 15, 1982.
- [3] L. J. Hornbeck, "Deformable mirror spatial light modulators," in Proc. SPIE, vol. 1150, pp. 86-102, 1990.
- [4] P. Lorrain, D. R. Corson, and F. Lorrain. Electromagnetic Fields and Waves. 3rd ed. W. H. Freeman and Company, New York, 1988.
- [5] D. R. Lide, ed. CRC Handbook of Chemistry and Physics. 71st ed. CRC Press, Boston, 1990.
- [6] K. K. Stevens. Statics & Strength of Materials. 2nd ed. Prentice-Hall, Englewood Cliffs, New Jersey, 1987.
- [7] M. R. Lindeburg, EIT Reference Manual, 7th ed., Professional Publications, Inc., CA, 1990.
- [8] T. H. Lin, "Implementation and characterization of a flexure-beam micromirror spatial light modulator," in Optical Engineering, vol. 33, pp. 3643-3648, Nov. 1994.
- [9] H. B. Palmer, "The Capacitance of a parallel-plate capacitor by the Schwartz-Christoffel transformation," in Electrical Engineering, pp. 363-366, March 1937.
- [10] P. M. Morse and H. Feshbach. Methods of Theoretical Physics. McGraw-Hill, New York, 1953.
- [11] M. Abramowitz and I. Stegun. Handbook of Mathematical Functions. Dover Publications, New York, 1972.
- [12] J. B. Marion and S. T. Thornton. Classical Dynamics of Particles & Systems. 3rd ed. Harcourt Brace Jovanovich, San Diego, 1988.
- [13] R. A. Serway. Physics for Scientists and Engineers. 2nd ed. Saunders College Publishing, Philadelphia, 1986.
- [14] T. A. Rhoadarmer, V. M. Bright, B. M. Welsh, S. C. Gustafson, and T. H. Lin, "Interferometric characterization of the flexure beam micromirror device," in Proc. SPIE, Vol. 2291, 1994, pp. 13-23.

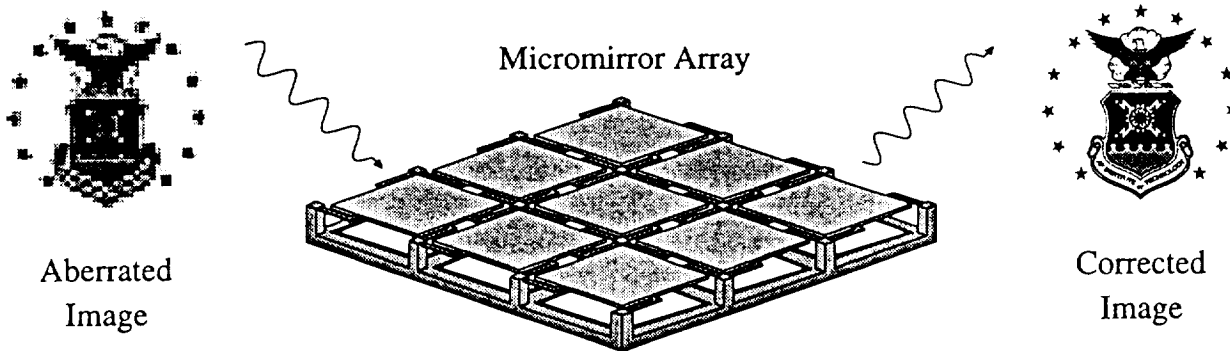


Figure 1. Use of Flexure-Beam Micromirror Devices in phase corrective optics.

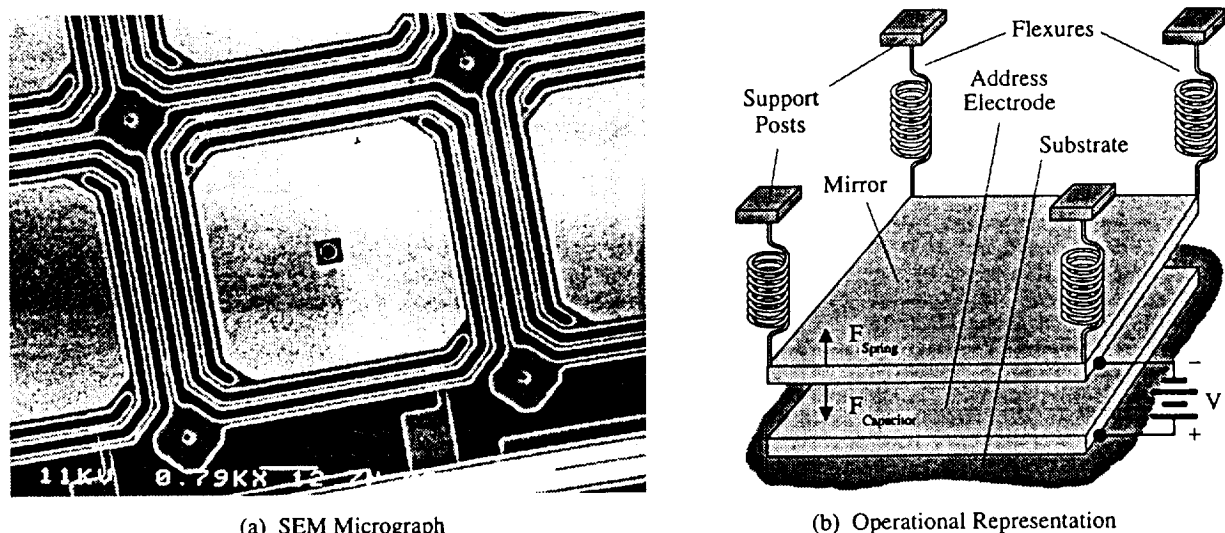


Figure 2. Micrograph and representation of the square Flexure-Beam Micromirror Device.

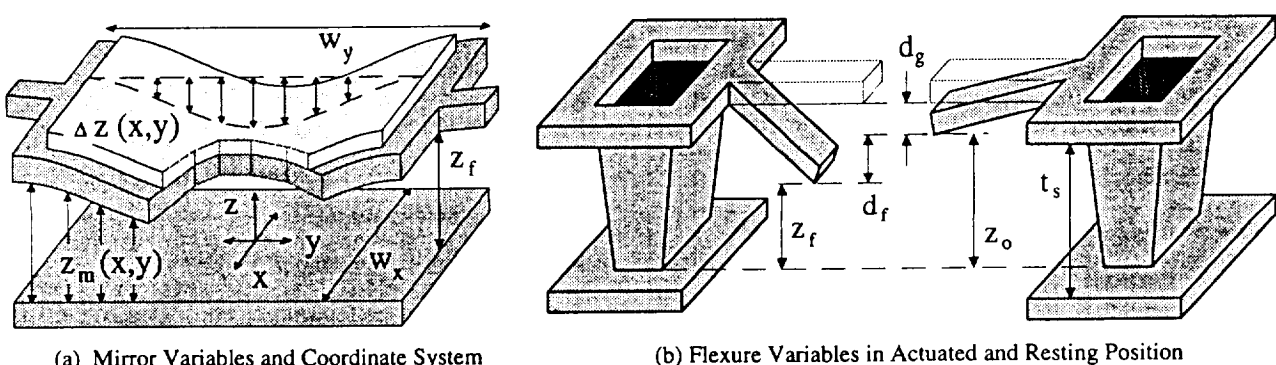
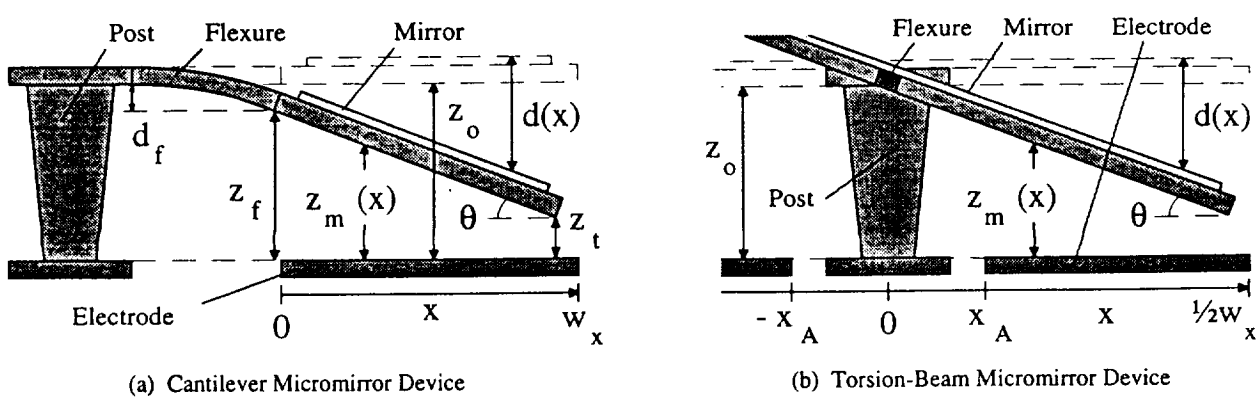


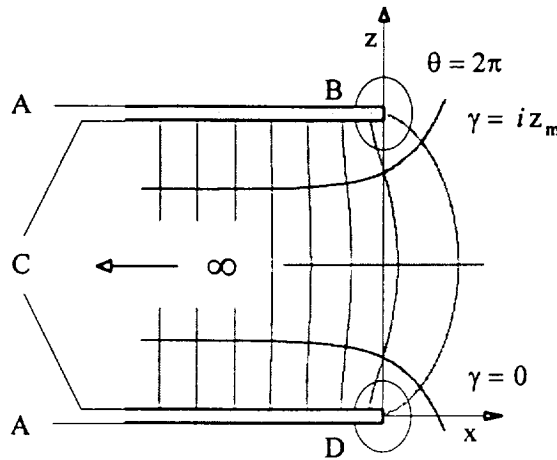
Figure 3. Graphical identification of micromirror device dimension variables and coordinate system.



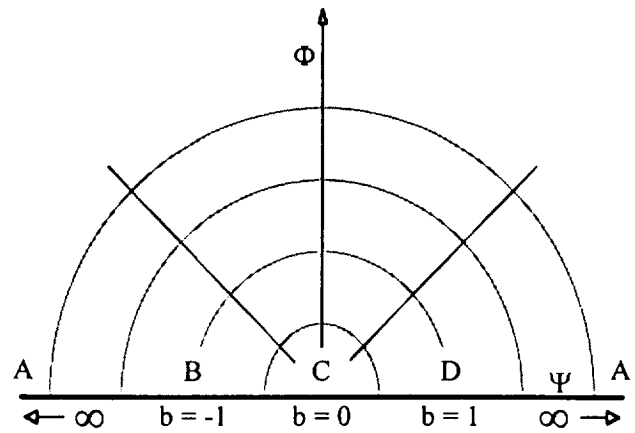
(a) Cantilever Micromirror Device

(b) Torsion-Beam Micromirror Device

Figure 4. Side view of the Cantilever and Torsion-Beam micromirror deflection with assigned variables.

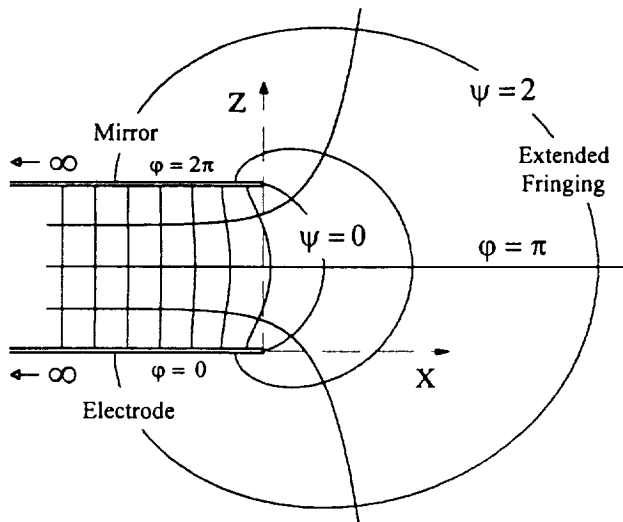


(a) Original $\gamma = x + iz$ Plane

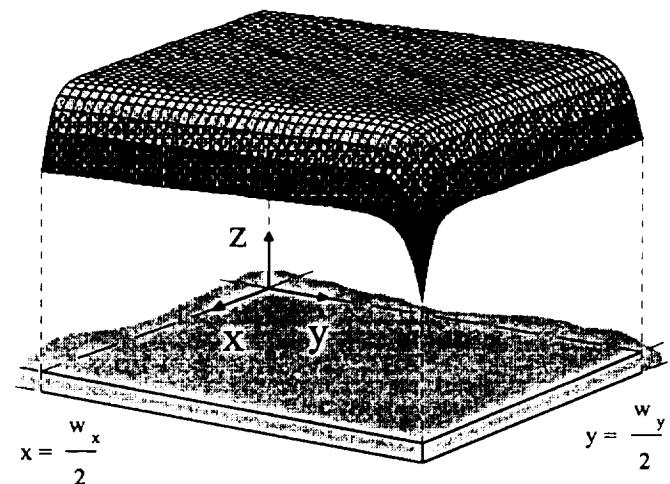


(b) Transformed $W = \Psi + i\Phi$ Plane

Figure 5. Origianl and transformed planes used in the Schwartz-Christoffel transformation of a parallel plate capacitor [10].



(a) Schwartz-Christoffel transformation solution



(b) Normalized fringing electric field magnitude

Figure 6. Electric field fringing analysis of a parallel-plate capacitor using the Schwartz-Christoffel transformation.

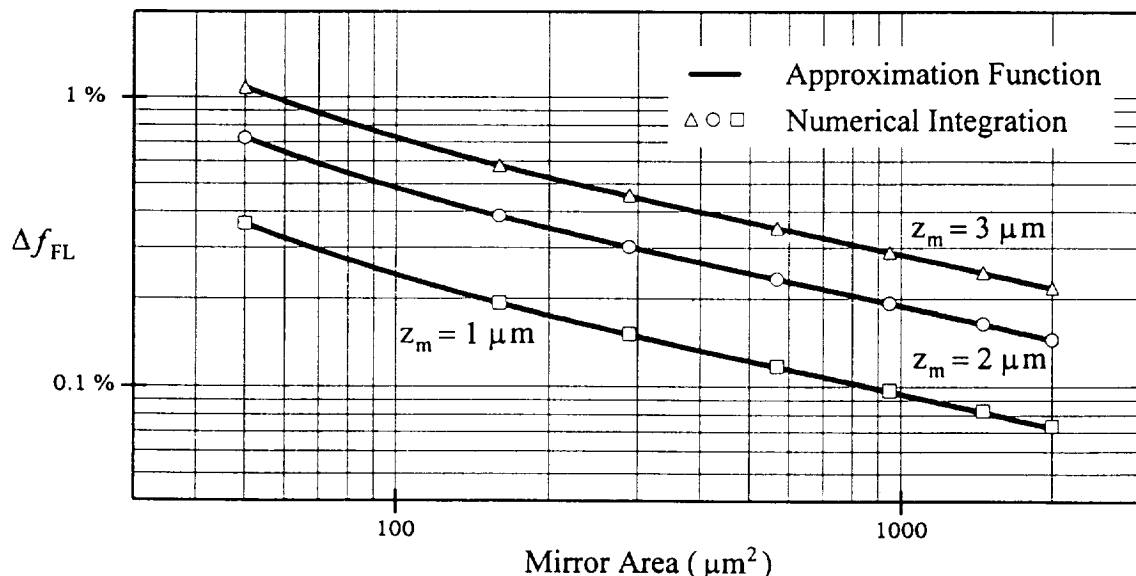


Figure 7. Plot of fringing loss approximation function with respect to mirror area along with numerical integration results.

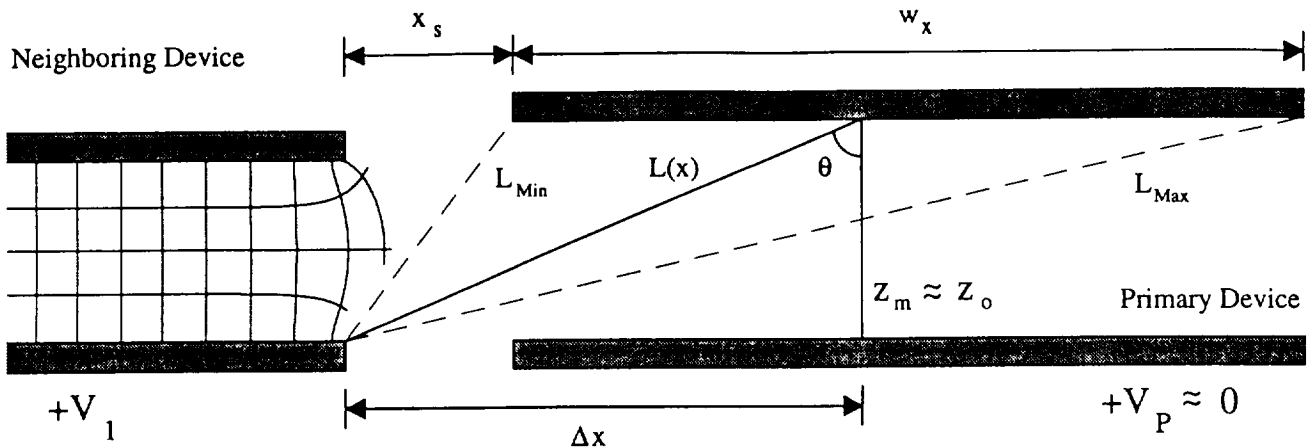


Figure 8. Range of cross-talk electric field lines of neighboring micromirror devices affecting primary device.

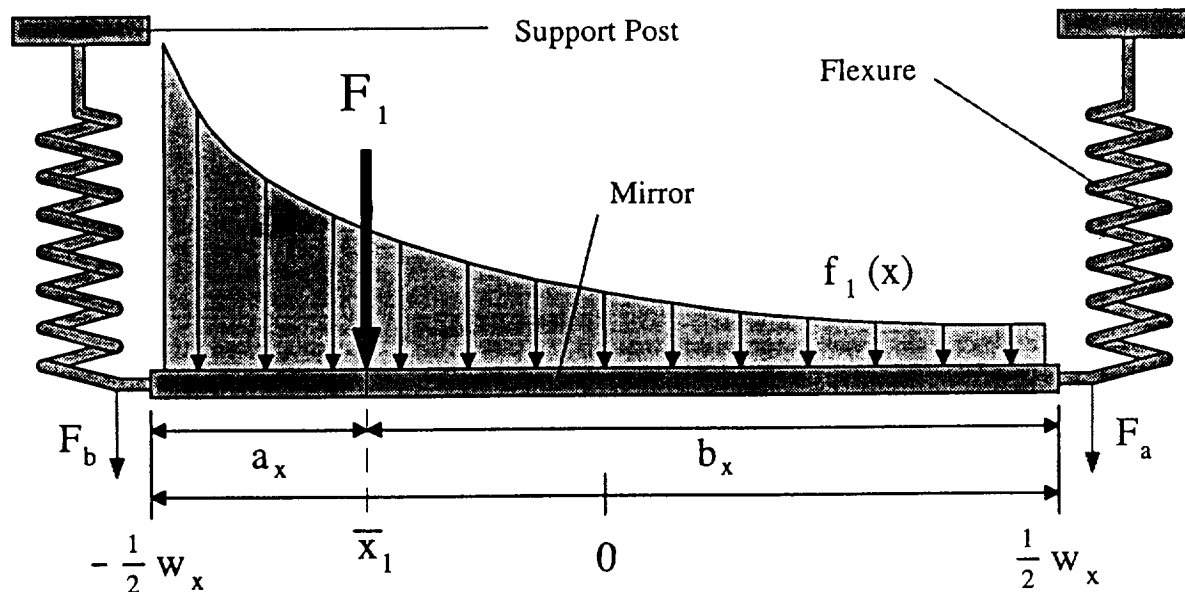


Figure 9. Cross talk linear force distribution along primary micromirror device and resulting forces at each end.

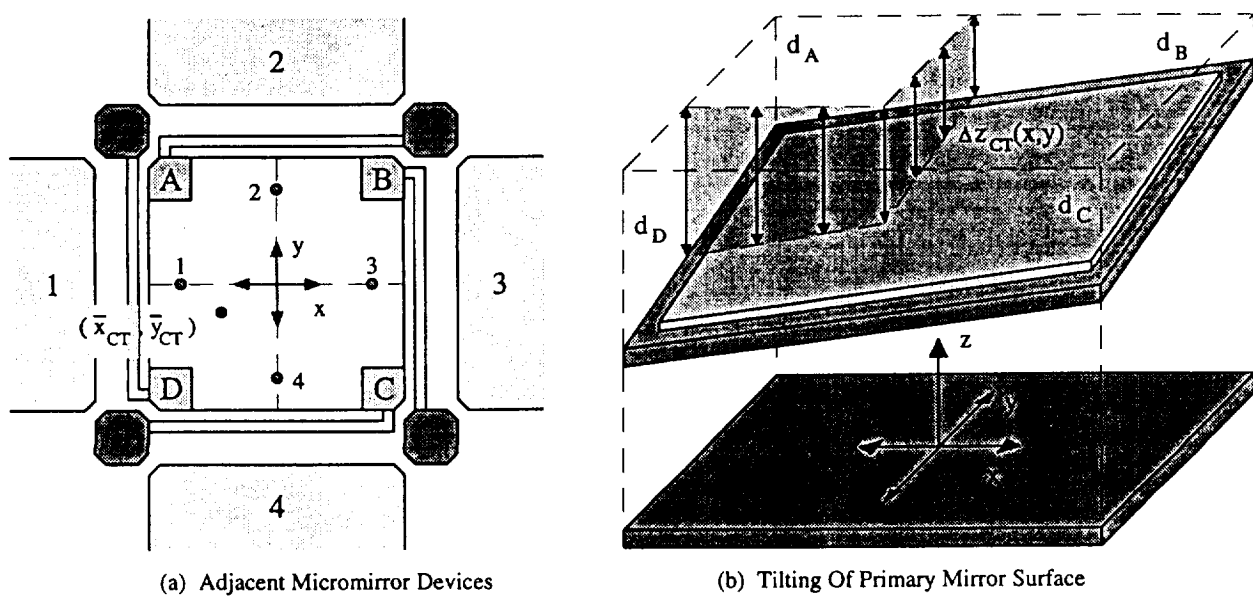


Figure 10. Cross-talk interference of adjacent devices and resulting mirror surface tilt of the primary mirror surface.

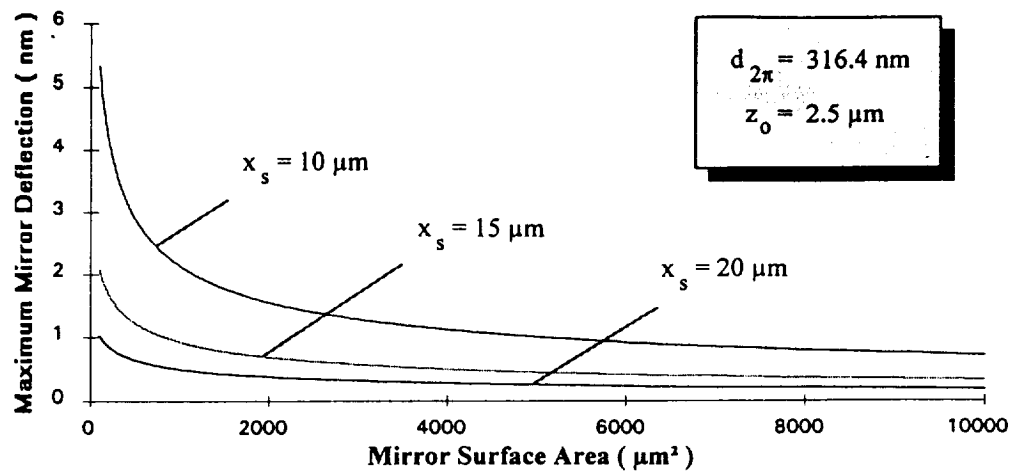


Figure 11. Plot of maximum deflection of primary mirror surface due to cross-talk versus micromirror area.

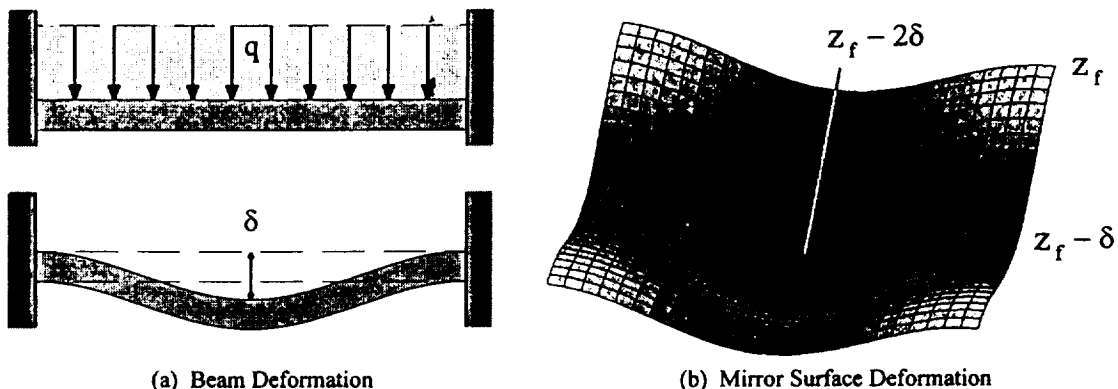


Figure 12. Use of beam deflection analysis along one dimension to represent mirror surface deformation along two dimensions.

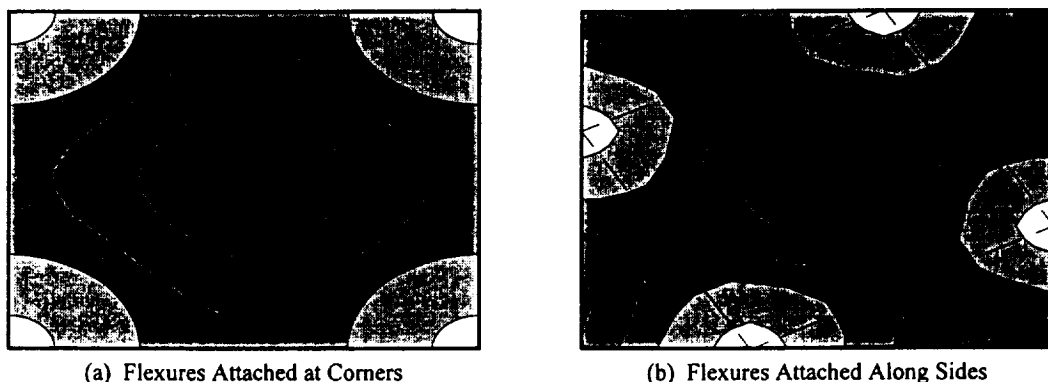


Figure 13. Plot of surface deformation function for a rectangular Flexure-Beam device with two flexure locations.

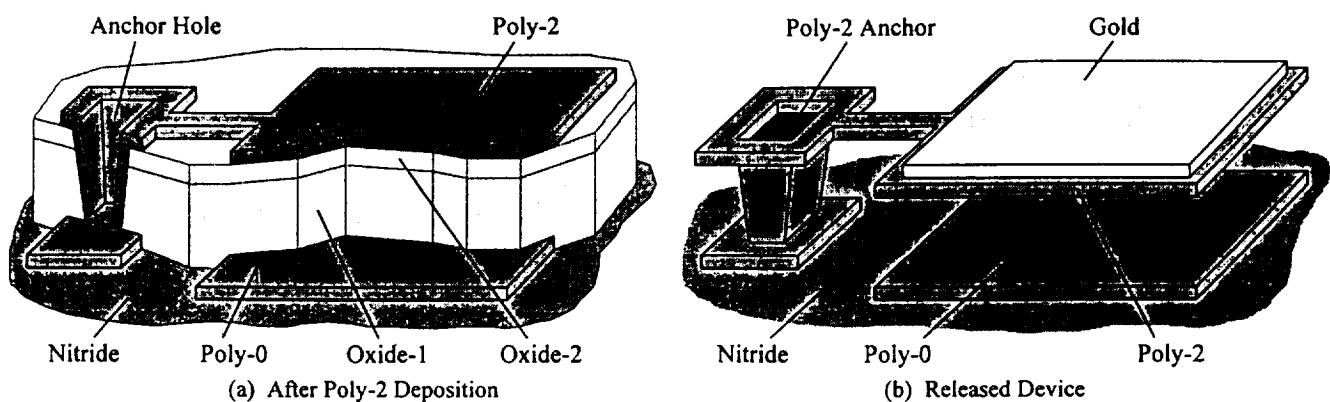


Figure 14. Graphical illustration of the MUMPS fabrication process using a simple Cantilever micromirror device.

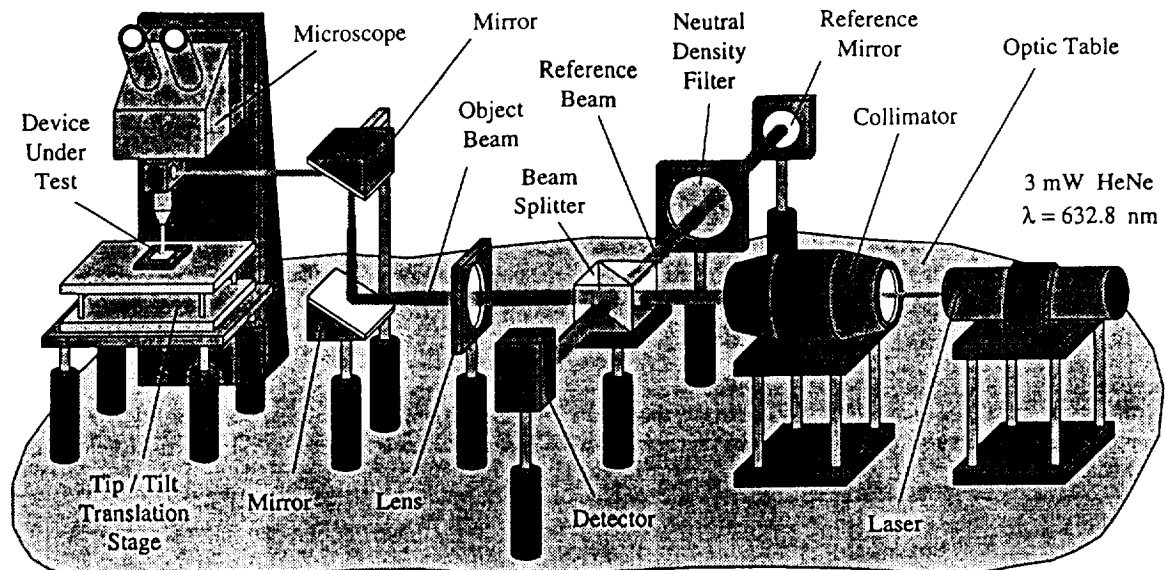


Figure 15. Experimental setup of the microscope-based laser interferometer.

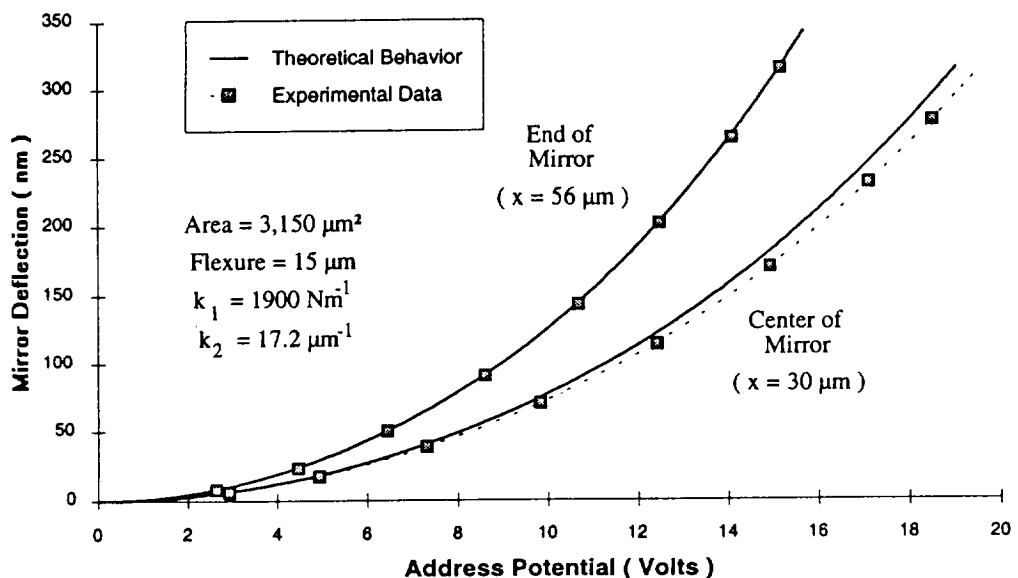


Figure 16. Characteristic behavior curves for two locations on the Cantilever micromirror device.

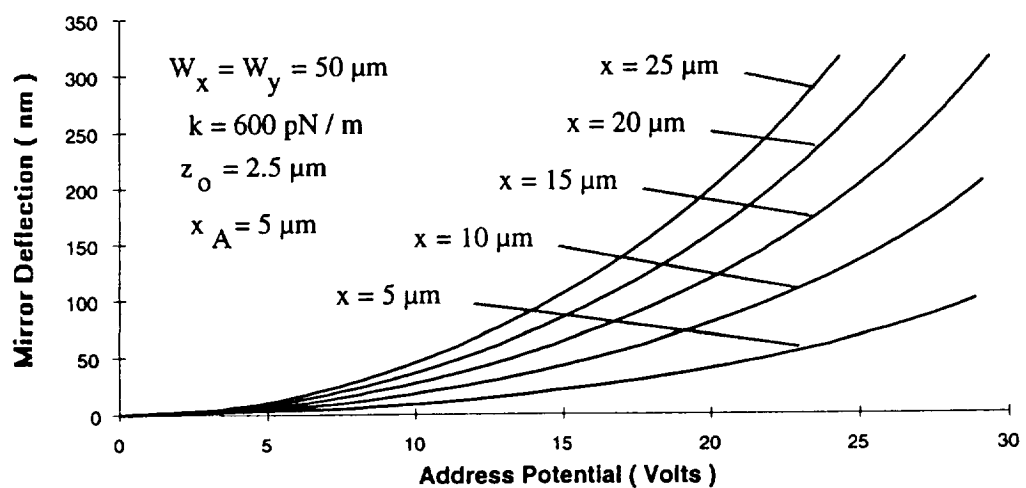


Figure 17. Characteristic behavior of a Torsion-Beam Micromirror Device at various positions along the surface.

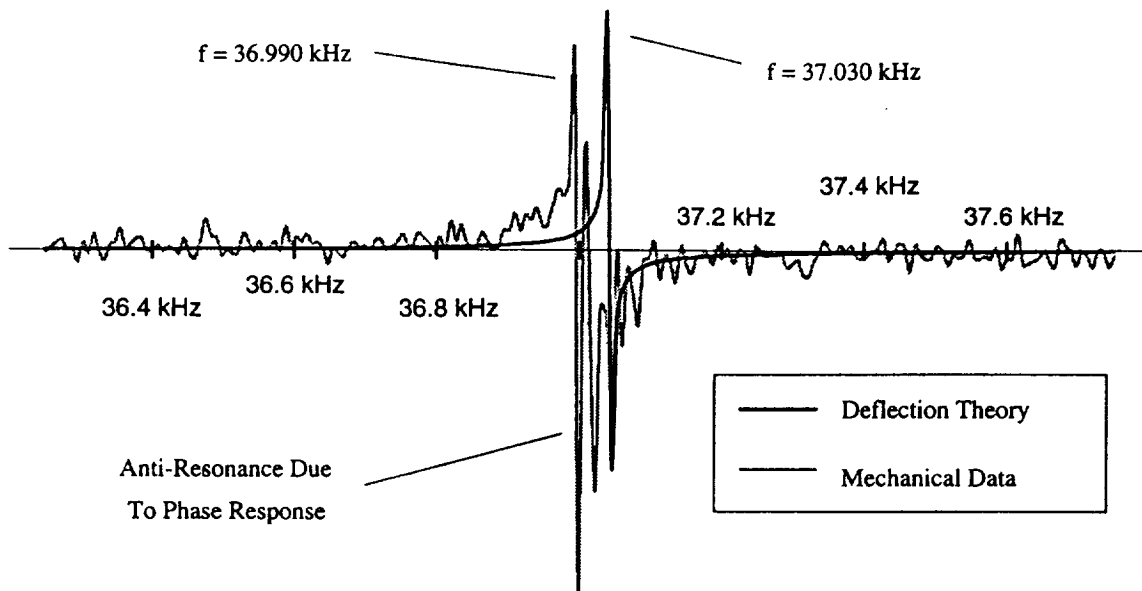


Figure 18. Theoretical and empirical frequency response of the square Flexure-Beam Micromirror Device.

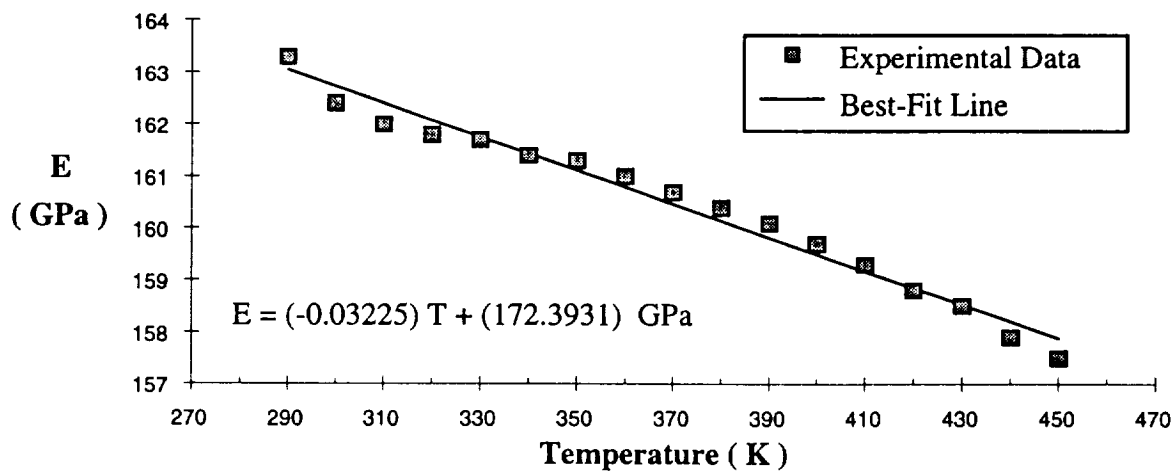


Figure 19. Elastic modulus as a function of temperature extracted from the square Flexure-Beam Micromirror Device.

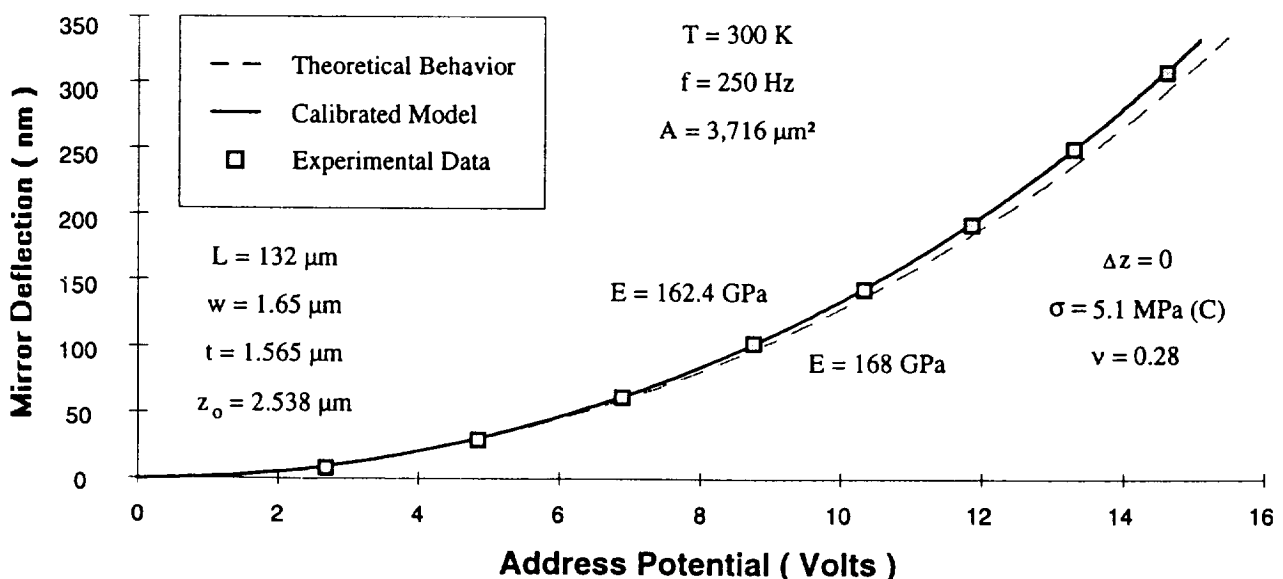


Figure 20. Theoretical and empirical characteristic behavior of the square Flexure-Beam Micromirror Device.